Electron temperature and density measurements in laser-produced large-scale-length gas-bag plasmas by x-ray spectroscopy

S. H. Glenzer, C. A. Back, K. G. Estabrook, B. J. MacGowan, D. S. Montgomery,* R. K. Kirkwood, J. D. Moody, D. H. Munro, and G. F. Stone

L-339, Lawrence Livermore National Laboratory, P.O. Box 808, Livermore, California 94551

(Received 12 August 1996; revised manuscript received 1 October 1996)

We present temporally and spatially resolved measurements of the *K*-shell emission from argon and chlorine dopants in laser-produced mm-size gas-bag plasmas. Particularly useful for the diagnostics of these plasmas are the line intensity ratios of the He- and H-like resonance lines to their respective Li- and He-like dielectronic satellite transitions. By Abel inverting the experimental spectra and applying time-dependent collisional-radiative modeling, local electron temperatures, and densities are deduced. About 0.4 ns after the beginning of the laser heating, we observe a homogeneous plasma center which heats steadily until the end of the heating pulse. Although the heating is slower than predicted by hydrodynamic simulations, the measured peak electron temperature of $T_e = 3$ keV for neopentane-filled gas bags is in good agreement with the hydrodynamic simulations. In addition, the electron densities inferred from the line intensity ratio of the intercombination to the resonance line of heliumlike argon are consistent with 10^{21} cm^{-3} as expected from the initial gas fill density. Further gas fill densities have been investigated, and in agreement with simulations we find lower temperatures for lower gas densities. [S1063-651X(97)05601-8]

PACS number(s): 52.70.La, 32.30.Rj, 52.25.Nr, 52.25.Vy

I. INTRODUCTION

Millimeter-size gas-bag plasmas are routinely produced with the Nova laser facility at the Lawrence Livermore National Laboratory to study laser-plasma interactions. The plasma conditions and the scale length of gas bags are expected to be similar to the corona of indirectly driven inertial-confinement fusion plasmas [1,2] which will be produced with the next generation of large laser facilities, e.g., with the National Ignition Facility (NIF). Stimulated scattering processes due to parametric instabilities in this plasma region, such as stimulated Brillouin scattering (SBS), stimulated Raman scattering (SRS), filamentation and the two-plasmon decay instability [3,4], can reduce or redirect the laser energy delivered to the fusion target and affect present target designs and laser specifications for the NIF [5,6].

In the present investigation we measured the temperature and density of gas-bag plasmas by x-ray emission spectroscopy [7]. Since the electron density, particle composition, and scale length of gas-bag plasmas are constrained by the gas fill and size of the target, the electron temperature is the most critical parameter to be determined experimentally. An accurate and independent measurement of the electron temperature and of the uniformity of the plasma is particularly important for the interpretation of current gas-bag experiments. For example, plasma parameters derived from the *K*-shell emission of Ar and Cl dopants are very useful for a comparison with the temperature and density sensitive *L*-shell emission spectra of Xe dopants [8] to test atomic modeling [9]. Other experiments studying the transmission of laser beams through gas-bag plasmas [10] depend critically on the electron temperature sensitive inverse bremsstrahlung absorption cross section. Furthermore, experiments are being performed to measure the amount of laser light scattering owing to parametric instabilities as a function of density and temperature of the plasma [11]. Finally, the correlation between SBS and SRS has been investigated, and the energy transfer between crossed beams via ion acoustic waves was measured [12] in gas-bag plasmas. The threshold for the onset of laser-plasma instabilities, their growth rate and the phase velocities of the accompanying plasma waves depend on plasma parameters such as electron temperature and density, and so accurate plasma characterization is an important part of understanding laser-plasma interaction experiments.

Some experiments were carried out previously using different types of gas-bag targets than those currently employed for the above-mentioned studies and for the present investigation. In those previous experiments spatially averaged temperatures were inferred from the ratio of the Ly-α lines (i.e., the $1s\,^2S$–$2p\,^2P^\circ$ transitions in hydrogenlike ions) of argon and chlorine dopants [13], and from the ratio of the He-α line (i.e., the $1s^2\,^1S$–$1s2p\,^1P^\circ$ transition in a heliumlike ion) of titanium to the Ly-α line of chromium, that were deposited on a fiber in the center of the target [14–16].

In this study we recorded the spectra of optically thin *K*-shell emission of argon and chlorine dopants in gas bags. In particular, the intensity ratios of the resonance transitions (He-α and Ly-α) of the heliumlike and hydrogenlike ions Ar XVII and Ar XVIII to their respective dielectronic satellite transitions ($1s^22p\,^2P^\circ$–$1s2p^2\,^2D$ or j,k,l satellites and $1s2p\,^1P^\circ$–$2p^2\,^1D$ [17,18]) were found to be very useful as a reliable determination of the detailed temporal evolution of the electron temperature of gas bags. For the typical gas-bag densities of 10^{21} cm^{-3} and temperatures of 3 keV, this method has several advantages over those of Refs. [13–16].

*Present address: Los Alamos National Laboratory, Los Alamos, New Mexico 87545.

The advantages are discussed in detail in Sec. III A. An important feature is that the intensities of lithiumlike dielectronic satellites closely follow electron temperature changes, so that less than a 0.1-ns lag occurs, thus providing an appropriate spectral feature to determine the temperature history of the gas-bag plasma independent of hydrodynamic simulations.

We present measurements of a large number of shots which enables us to ascertain that the reproducibility of the plasma conditions is found to be about 15%. From spatially resolved line intensity measurements, local emission coefficients are inferred by Abel inversion and local temperatures are obtained with a resolution of 110 μm. The results show that gas-bag plasmas have a homogeneous center with a diameter of 2 mm. The results are in good agreement with the hydrodynamic code LASNEX [19]. In addition, we compare temperatures inferred from dielectronic satellite transitions with those of other line ratios arising from the K-shell emission from argon and chlorine. In particular, we compare to the isoelectronic ratio of the He-β lines (i.e., the $1s^2\,{}^1S-1s3p\,{}^1P^\circ$ transitions in heliumlike ions) of argon and chlorine [16,20,21]. This method is presently employed for the diagnostics of several targets at Nova. Other line ratios, e.g., the ratio of Ly-α transitions of both ions, do not follow fast temperature changes on a time scale smaller than 1 ns. Although they are generally in agreement with the temperatures derived from the more appropriate ratios, they are not used in this study.

We also performed a spectroscopic density determination from the ratio of the intercombination line to the resonance transition of heliumlike argon. This line intensity ratio was shown to be useful for density diagnostics in Ref. [22], where a well-diagnosed θ pinch discharge had been used as plasma source. This line intensity ratio is employed for the diagnostics of, e.g., laser-produced plasmas [23,24], z pinches [25–27], and plasma jets [28]. Here we find electron densities consistent with hydrodynamic simulations and with measurements [1] of the Raman scattered light. The densities obtained in this way are also consistent with the line intensity ratio of the fine structure components of the Ly-α transitions in Ar XVIII.

II. EXPERIMENT

A. Gas-bag targets and laser illumination

Gas bags are nearly spherical volumes of gas at typically one atmosphere pressure. Two 0.35-μm-thick polyimide ($C_{14}H_6O_4N_2$) membranes are mounted on each side of a 0.4-mm-thick aluminum washer with an inner diameter of 2.75 mm. The inner volume is inflated with gas, typically neopentane (C_5H_{12}), forming the nearly spherical balloon. The membranes extend to a minor diameter of 2.5 mm orthogonal to the washer surface [Fig. 1(a)]. When inflated, the thickness of the membranes is about 0.22 μm. For spectroscopic measurements we used 1% argon and 1% freon-13 ($CClF_3$) dopants added to the main gas. The gas concentrations are measured by mass spectrometry for each batch of mixed gas.

The gas bags are heated with 9 beams of the Nova laser [29], a Nd:glass laser operating at 1.053 μm. For the heating of gas bags the laser light is frequency tripled to $\lambda = 351.1$ nm. $f/4.3$ focusing optics are used defocused by 6.78 mm. This configuration results in laser beams converging at the center of the gas bags with a laser spot size of each individual beam of 1.7-mm diameter on the surface of the gas bag [13]. A total-energy of 21 kJ is delivered in a 1-ns square pulse, giving an averaged intensity of 10^{14} W cm^{-2} per beam.

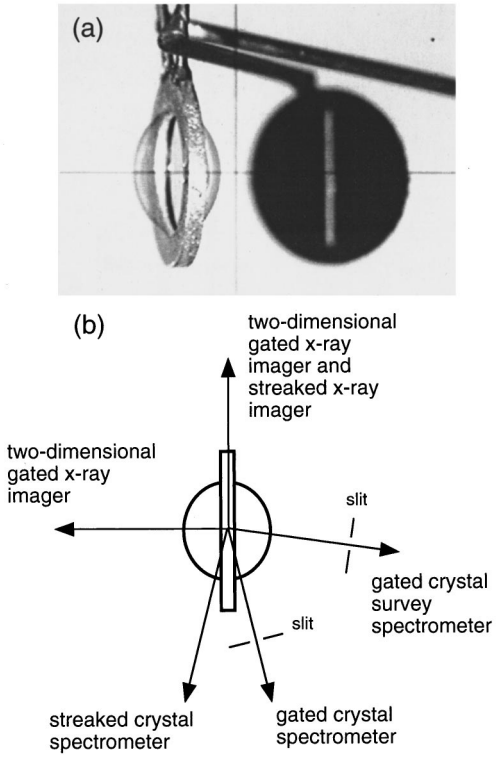

FIG. 1. Example of a gas-bag target with two vertical slits mounted at a distance of 8 mm from the gas-bag center. The thickness and the inner diameter of the washer are 0.4 mm and 2.75 mm, respectively (a). Experimental setup showing the view of the x-ray diagnostics on the gas-bag plasma (b).

When the membrane of the gasbag is first irradiated by the laser, it heats and quickly ablates similar to an exploding foil [30]. The cold gas behind the membrane is then dissociated and first ionized by multiphoton ionization [31]. Then efficient heating of the plasma by inverse bremsstrahlung occurs until the gas becomes less opaque, allowing the laser to penetrate further into the plasma. Four hundred picoseconds after the beginning of the heating a homogeneous spherical plasma (see Sec. III A) has formed. The exploding membrane launches a weak shock into the gas traveling to the gas-bag center with the sound speed. Simulations show that electron densities and ion temperature in the shock are a factor of 2 higher than the average values in a gas bag. On the other hand, the effect of the shock on the electron temperature is negligible for the 0.22-μm-thick membranes. In previous experiments larger perturbations of the plasma have been observed with a 0.4-μm-thick membrane [13]. The dopants reach the hydrogenlike and heliumlike ionization stages and the bulk gas is fully ionized about 0.2 ns after the beginning of the heating (t_0), resulting in an averaged electron density of $n_e = 10^{21}$ cm^{-3} for neopentane.

We performed hydrodynamic two-dimensional, cylindrical symmetric simulations of the plasma evolution with the

code LASNEX [19]. The laser is modeled by typically 1000 rays per beam assuming absorption by inverse bremsstrahlung including effects of laser-induced non-Maxwellian electron distributions [32]. For gas-bag plasmas this effect reduces electron temperatures by about 3%. Electron heat transport is by diffusion with a flux limiter of 0.05. The calculations do not critically depend on the flux limiter. For example, increasing the flux limiter to 0.1 results in a 6% lower temperature. Nine heater beams with a total of 21 kJ at 3ω were modeled, and one interaction beam delayed by 0.5 ns with 500 J at 3ω was along the axis of symmetry. Further simulations were performed with heater beam energies reduced by 22% for neopentane filled gas bags and 31% for propane filled gas bags. These values correspond to the measured energy losses by SBS and SRS sidescattering and backscattering of the unsmoothed heater beams. Nonlocal thermodynamic equilibrium rate equations determined the ionization state and calculations of an atomic spectra model were used for the emissivities and opacities included in multigroup diffusive photon transport.

Unlike the more traditional targets for high-density laser-plasma interactions (solid or exploding foil targets) the gas bag targets convert most of the incident laser energy into thermal energy of the electrons and less into the kinetic energy of bulk plasma motion. The energy budget for a typical gas-bag simulation is 22 kJ incident, 12.5 kJ absorbed, 8.8 kJ in electron thermal energy ($T_e = 3.3$ keV) and only 2.6 kJ in kinetic energy (21% of absorbed energy). These numbers should be compared with typical exploding foil plasmas where similar calculations (to produce a 10% n_{cr} plasma where the critical density is given by n_{cr} (cm^{-3}) $= 1.1\times 10^{21}/[\lambda(\mu\mathrm{m})]^2$) show 22 kJ incident, 8 kJ absorbed, 3.1 kJ in electron thermal energy ($T_e = 2.4$ keV) and 4.5 kJ in kinetic energy (56% of absorbed energy). The heating of a stationary low-density target is therefore a much more efficient way of producing a high-temperature plasma with the added benefit that density and velocity gradients are much less severe and therefore more suitable for experiments that mimic laser plasma interactions within indirectly driven inertial confinement fusion hohlraums.

B. Diagnostic techniques

For spectroscopic electron temperature measurements we observe the plasma emission through a crossed slit configuration. A slit of 3-mm height and 150-μm width cut in a copper shield (300 μm thick, 3 mm in diameter) is mounted on the target at a distance of 8 mm, effectively limiting the plasma size seen by the spectrometer [Fig. 1(a)]. This slit allows a view through the gas-bag center. At a distance of 11.9 cm from the first slit we used four parallel slits (250-μm width, 2-mm height) to image the emission onto four parallel strips of a gated microchannelplate (MCP) detector with a factor of 2 magnification. Between the four slits and the microchannelplate a pentaerythritol crystal is mounted at the Bragg angle to spectrally disperse the plasma emission. We used curved crystals to obtain survey spectra and various flat crystals for measurements with higher resolution. Since source broadening is efficiently reduced by the first slit, a resolution of $\lambda/\Delta\lambda = 800$ is achieved by this type of spectrometer [33].

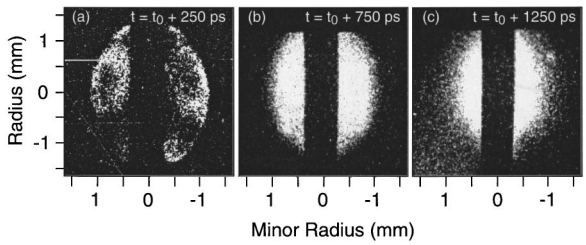

FIG. 2. Two-dimensional x-ray pinhole images of the emission of neopentane-filled gas bags with energies $E > 2$ keV for three successive times of a single shot. The images were taken edge-on to the washer, and their central part is blocked by the washer and an additional shield which is mounted on the washer. In (a) at $t = t_0 + 0.25$ ns the imprint of the laser beams can be observed (t_0 indicates the beginning of the laser heating). In (b) at $t = t_0 + 0.75$ ns the plasma emission is homogeneous, and in (c) at $t = t_0 + 1.25$ ns the radius of the emission region is slightly reduced because of the shock front moving toward the gas-bag center. During this time no significant deformation from a spherical symmetry or refraction of the plasma can be observed.

The gated MCP detector [34,35] has four sensitive rectangular strips (4×40 mm^2). A gate pulse of 0.08-ns square traverses the length of the strip along the wavelength dispersion direction in 0.25 ns. This pulse results in a time resolution of 0.1 ns for the measurements of the dielectronic satellite spectra, because the lines of interest are only 3 mm apart on the MCP. The four strips can be timed independently. We chose a time delay of 0.25 ns between the strips, thus covering with four successive measurements the temporal evolution of the gas-bag plasma, which is produced with a 1-ns square pulse. At the output of the MCP a P20 phosphor is mounted, and its illumination is recorded on film (Kodak TMAX 3200), which we digitized with a resolution of 22 μm.

Four further diagnostics were fielded observing the x-ray emission of gas-bag plasmas [Fig. 1(b)]. Two pinhole (10 μm) cameras with gated x-ray MCP detectors [35,36] give two-dimensional images of the emission with radiation energies of $E > 2$ keV. They observe the target parallel and orthogonal to the washer surface measuring the size of the plasma. In general, these images show that after $t = t_0 + (0.3 \pm 0.1)$ ns the plasma is homogeneous and of nearly spherical symmetry. Figure 2 shows an example of the measurements. On the images taken in the first 0.3 ns of the experiment, the imprints of the laser beams are observed. The central hole of the Nova laser beams can be clearly identified in Fig. 2(a). Before the focusing lens the beam diameter is 68 cm, and the central part of 19-cm diameter is blocked. These measurements verify the alignment of the laser beams and monitor the illumination and heating of the plasma. Further successive images from the same shot demonstrate the plasma homogeneity, and show no significant deformation of the plasma during the first nanosecond [cf. Figs. 2(b) and 2(c)].

A x-ray streak camera observed the shock front propagating through the plasma. Figure 3 shows a measurement of the x-ray emission filtered for energies $E > 2$ keV of a gas bag as a function of time. A slit before the streak camera with 10-μm width was used to image the center of the gas bag onto the photocathode. In this way spatial resolution is

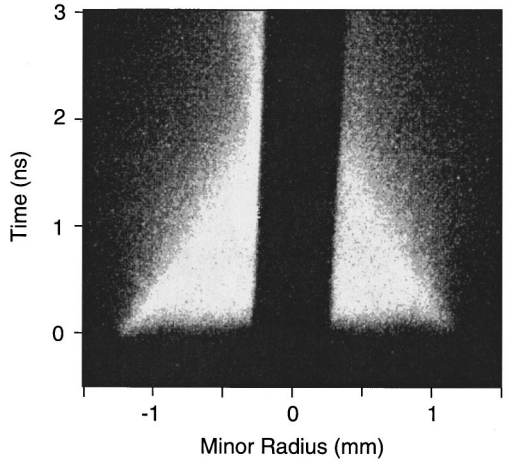

FIG. 3. Streak camera measurement of the emission of a neopentane-filled gas bag with energies $E>2$ keV. The measurement was taken with the same angle of observation as Fig. 2, and the spatial resolution is along the midplane of the gas bag. The emission region of the plasma moves toward the center of the gas bag with a velocity of $v=5\times10^7$ cm/s.

achieved only along the horizontal direction. A ten times magnification was used, and the temporal resolution of this measurement is 25 ps. The emission front or blast wave propagates with a velocity of 5×10^7 cm/s toward the center of the gas bag (Fig. 3). The solution of the kinetic dispersion relation [37] shows that for a CH plasma with a temperature of 3 keV this velocity coincides with the sound speed of the plasma. At about $t=t_0+2.5$ ns the shock reaches the center of the gas bag.

We also fielded a crystal spectrometer coupled to a x-ray streak camera which detects the resonance lines of heliumlike and hydrogenlike argon and chlorine with a temporal resolution of 25 ps. The spectra are source broadened, so that the satellite and intercombination lines cannot be resolved. These data are useful to monitor the reproducibility of the temporal evolution of the plasma emission.

III. EXPERIMENTAL RESULTS AND DISCUSSION

A. Electron temperature

Figure 4 gives an example of a film record showing a survey spectrum of the K-shell emission of argon and chlorine in the wavelength range of 0.33 nm$<\lambda<$0.46 nm. The spectrum is detected at $t=t_0+0.6$ ns, about 0.4 ns before peak temperature. A lineout is taken in the center averaging over 110 μm along the height of the gas-bag plasma. The lineout has been corrected for the wavelength-dependent instrument response [38], filter transmission, and crystal reflectivity [39]. The He-β (0.3365 nm), Ly-α (0.3737-nm), and the He-α (0.3949 nm) spectral lines of argon and He-β (0.3790 nm), Ly-α (0.4188 nm), and the He-α (0.4444 nm) spectral lines of chlorine are easily identified [40,41]. On the red wings of the Ly-α spectral lines, we also observe weak $1s2\ell-2\ell2\ell'$ dielectronic satellite transitions and on the red wings of the He-α spectral lines we observe the $1s^2\,{}^1S-1s2p\,{}^3P^\circ$ intercombination lines plus $1s^22\ell-1s2\ell2\ell'$ dielectronic satellite transitions. The satellite feature on the red wing of the He-α line is dominated by the j,k,l satellites. The upper levels of the j,k,l dielectronic satellite transitions are primarily populated by the capture of a free electron e by an ion (dielectronic capture satellites),

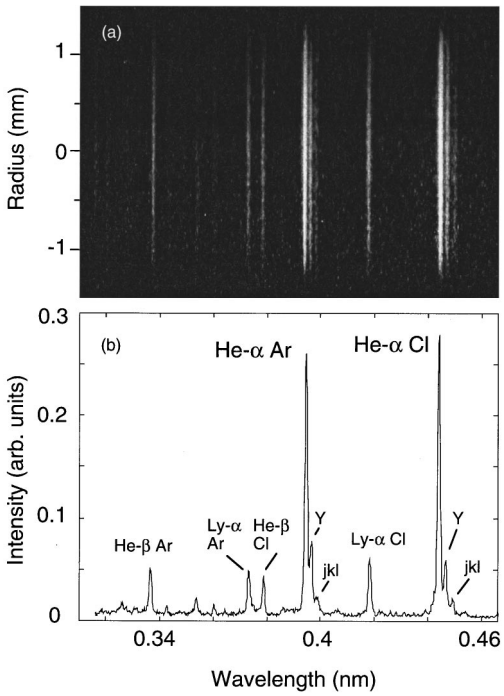

FIG. 4. Example of the film showing a survey spectrum of the K-shell emission of Ar and Cl dopants of a neopentane-filled gas bag (a). Spatial resolution is in the vertical direction, and spectral resolution in the horizontal direction. A lineout averaging over 110 μm of the gas-bag emission shows the typical emission pattern consisting of the He-β, Ly-α, and He-α lines of argon and chlorine (b).

$$1s^2+e\rightarrow1s2\ell'n\ell''. \tag{1}$$

The ion in the double excited state has two decay channels. It can autoionize with emission of one electron to the continuum, giving rise to resonance excitation, or it can stabilize by radiative decay, producing the observed dielectronic satellite line emission. The dielectronic satellites occur on the red wing of the resonance lines due to the screening of the excited $n\ell$ electron. As pointed out by Gabriel [17], the temperature dependence of the dielectronic recombination rate differs from that of the electron collisional excitation rate of the resonance lines. Therefore, the relative intensities of the dielectronic satellite transitions compared to their close-lying resonance lines are very useful for electron temperature measurements. This is demonstrated in Fig. 5, where we show steady-state collisional-radiative model calculations of the line intensity ratios of the He-α line of argon to the j,k,l dielectronic satellite transitions and of the Ly-α line of argon to the $1s2p\,{}^1P^\circ-2p^2\,{}^1D$ satellite as a function of the electron temperature. The two rates (dielectronic recombination and collisional excitation) have the same density dependence and, therefore, these line ratios are not sensitive to electron density variations (cf. Fig. 5). Electron density sensitive satellite ratios often involve innershell excitation from lithiumlike ions

$$1s^22\ell+e\rightarrow1s2\ell'n\ell''+e. \tag{2}$$

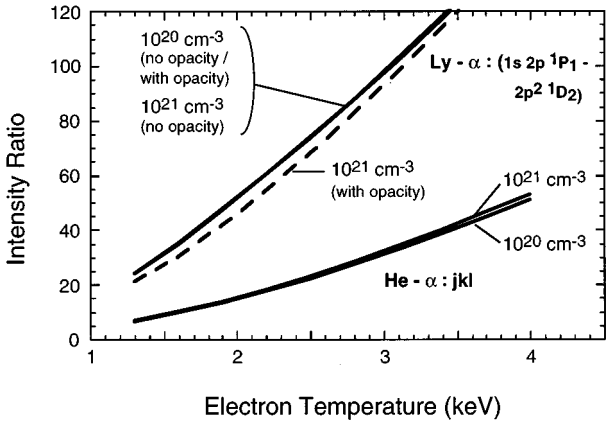

FIG. 5. Steady-state collisional-radiative model calculations for the argon K-shell emission [42]. The line intensity ratios of the He-α line (bottom) to the j,k,l dielectronic satellite transitions and of the Ly-α line (top) to the $1s2p\,^1P^\circ-2p^2\,^1D$ satellite are shown as a function of the electron temperature for electron densities of $n_e=10^{20}$ and 10^{21} cm^{-3}. For the argon densities in gas bags the ratio of the He-α line to the j,k,l dielectronic satellites shows no opacity (self-absorption) effects. Including opacity only the ratio of the Ly-α line to the $1s2p\,^1P^\circ-2p^2\,^1D$ satellite is affected for 10^{21} cm^{-3}, resulting in a slightly smaller ratio for the whole temperature range.

For example, the population densities of the upper levels of the a,q dielectronic satellites (see below) are affected by this mechanism.

Intensities of dielectronic satellite transitions were widely employed to diagnose laser-produced plasmas [24,43], micropinch discharges [44,45], and plasma foci [25]. The wavelengths, atomic transition probabilities or satellite line strengths of the dielectronic satellite transitions were calculated in a number of theoretical studies [17,18,46,47], and advanced calculations for relevant electron collision cross sections (e.g., Ref. [48]) have been performed. Atomic data of this type were used for the analysis and spectral modeling [42] of the present experimental data. They have been tested in low density plasmas, where electron temperatures were determined independently by nonspectroscopic techniques [49,50].

The analysis of the spectral line ratios was performed by time-dependent collisional-radiative modeling. In order to take into account the contributions of all relevant population mechanisms from an almost complete number of atomic states in the hydrogenlike, heliumlike, and lithiumlike ionization stage, we used the code FLY [42]. Lithiumlike dielectronic satellite transitions with the upper-state configuration $1s2\ell2\ell'$, and heliumlike dielectronic satellites with $2\ell2\ell'$, are taken into account. In this code, radiation transport is included by an escape factor approximation. However, the concentration of the gas dopants in gas bags is chosen to obtain optically thin argon and chlorine K-shell emission in the temperature range of interest. In particular, our calculations show that the inclusion of radiative transport effects (self-absorption) does not affect the intensity ratio of the He$-\alpha$ transition to the j,k,l dielectronic satellites of argon for $T_e>1.5$ keV. For electron densities of 10^{21} cm^{-3} the intensity ratio of the Ly-α line of argon to the $1s2p\,^1P^\circ-2p^2\,^1D$ satellite shows radiative transport effects of the order of 10% (cf. Fig.5).

In the present study the atomic modeling was carried out using a Maxwellian electron velocity distribution function. A modification of the electron impact excitation rates due to the effect of suprathermal electrons was not performed. For gas-bag plasmas approximately 3% of the laser energy of the heater beams is converted into hot electrons, e.g., as a secondary product of SRS. We measure a hot electron fraction of about 1% with temperatures of 17 keV by observing the bremsstrahlung in the x-ray spectral region with calibrated diodes [1]. It has been shown that the line intensity ratio of the He-α line to the j,k,l dielectronic satellites, which is used in this investigation for temperature measurements, is not sensitive to hot electron excitation for bulk electron temperatures of $T_e>1$ keV [51]. However, hot electrons can be seen to modify inner-shell excited dielectronic satellites, i.e., the a,q dielectronic satellite transitions, and the intercombination line [27,51]. In addition, satellites from double excited states where at least one electron has the configuration $n\ell$ with $n>2$ are not taken into account in the analysis. Therefore, we require high spectral resolution to determine the satellite contributions other than the j,k,l dielectronic satellites; see Fig. 4.

Figure 6 shows two high-resolution measurements in the wavelength region of the He-α spectral line of argon detected at $t=t_0+0.55$ ns and $t=t_0+0.80$ ns. From measurements of this type we deduce the line intensity ratio of the He-α to the j,k,l satellites with an error of less than 10%. This is achieved by fitting the measured data as shown in Fig. 6. We obtain a good fit of the detailed satellite structure, taking wavelengths from Ref. [47]. Ten individual lines have been included in the fit where the line profiles were assumed to be equal. The contribution of all $n=3$ satellites are approximated by a single profile, but with a larger width than the other lines. The line profile used in the fit is a Voigt function with 0.004-nm Gaussian and 0.002-nm Lorentzian width, and it represents essentially the instrument function of the detector. The dominant features are the He-α (or W) line (0.3949 nm), the $n=3$ dielectronic satellites (0.3955 nm), the intercombination (or Y) line: $1s^2\,^1S-1s2p\,^3P^\circ$ (0.3969 nm), the a,q,r (0.3967–0.3986 nm) dielectronic satellites, the k dielectronic satellite (0.3990 nm), and the combined j, l dielectronic satellites (0.3994 nm). The contribution of the l satellite to the feature at $\lambda=0.3994$ nm is 5%, and is included in the collisional-radiative modeling. We find only small deviations from the experimental data and the fit. On the blue wing of the He-α spectral line, the experimental data show a feature which is not taken into consideration by the fit. This could be due to a berylliumlike $1s2p^3-2s^2\,2s^2$ [52] or a lithiumlike $1s^2\,3\ell-1s2\ell'3\ell$ [53] satellite transition. A blue satellite was also observed in Mg IX in a micropinch discharge [54]. Another deviation occurs on the red wing of the resonance transition in a wavelength region close to the $n=3$ dielectronic satellite transitions, that is probably due to the fact that we approximated the $n=3$ dielectronic satellite structure by a single line.

The fit and the analysis focus on satellites with $n\leqslant3$ spectator electrons. The justification for ignoring other transitions is as follows: The $1s^2\,^1S-1s2s\,^3S$ spin-forbidden (or X) line at $\lambda=0.3994$ nm coincides with the j satellite. However, its intensity is negligibly small [55]. The results of the

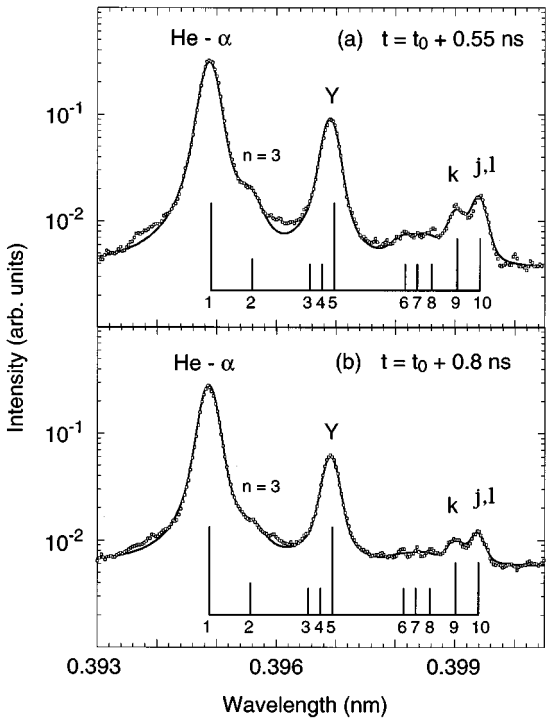

FIG. 6. High-resolution spectra of the heliumlike resonance line, intercombination line, and dielectronic satellites of argon at $t=t_0+0.55$ ns and $t=t_0+0.8$ ns. The spectra were taken from a neopentane-filled gas bag and represent emission averaged over 110 μm along the height of the gas-bag plasma: □. To determine the relative intensities of the argon spectral lines the spectrum was fit by ten lines (—): 1, He-α or $1s^2\,{}^1S_0-1s2p\,{}^1P_1$; 2, $n=3$ dielectronic satellites; 3, m or $1s^22p\,{}^2P_{3/2}-1s2p^2\,{}^2S_{1/2}$; 4, s,t or $1s^22s\,{}^2S_{1/2}-1s(2s2p\,{}^3P)\,{}^2P_{3/2,1/2}$; 5, Y or $1s^2\,{}^1S_0-1s2p\,{}^3P_1$; 6, q or $1s^22s\,{}^2S_{1/2}-1s(2s2p\,{}^1P)\,{}^2P_{3/2}$; 7, a or $1s^22p\,{}^2P_{3/2}-1s2p^2\,{}^2P_{3/2}$; 8, r or $1s^22s\,{}^2S_{1/2}-1s(2s2p\,{}^1P)\,{}^2P_{1/2}$; 9, k or $1s^22p\,{}^2P_{1/2}-1s2p^2\,{}^2D_{3/2}$; 10, j,l or $1s^22p\,{}^2P_{3/2,3/2}-1s2p^2\,{}^2D_{5/2,3/2}$.

collisional-radiative modeling show for our plasma conditions that its intensity is five orders of magnitude smaller than that of the j satellite. Furthermore, with increasing principal quantum number of the spectator electron, the wavelength of the respective dielectronic satellite transitions ($n=4$, etc.) are too close to the resonance line to be experimentally resolved. Fortunately, their contribution to the intensity of the He-α line is negligible. It was shown in Ref. [17] that with increasing nuclear charge Z, dielectronic satellites with $n>2$ spectator electrons become less important. According to that work for $Z>14$, $n=3$ dielectronic satellites have become negligible. In the present study the $n=3$ satellites are intense enough to determine their magnitude independently. However, the statement of Ref. [17] is consistent with our observations (Fig. 6), as the relative contribution of the $n=3$ satellites to the intensity of the He-α line is only 3.5%. Based on this observation, we expect satellites with the configuration $n\ell$ with $n>3$ to be less intense, and we have neglected those in the analysis.

The measurements shown in Fig. 6 are performed with a spatial resolution of 50 μm along the height of the gas bag. Since the plasma is symmetrically heated and the measurements are performed at an angle of 14° to the washer axis, a cylindrical symmetry for the plasma is assumed, allowing an Abel inversion of the measured intensities. To ensure the accuracy of the Abel inversion procedure, we tested different techniques. For example, we fit the radial intensities by a polynomial and performed the inversion by analytical integration. However, this procedure turned out to be too sensitive to small discrepancies between the measured intensities and the fit. Thus, especially in the center of the gas bag, the slope of the data becomes small, leading to large uncertainties in the local emission coefficients. Significantly smaller errors were achieved by dividing the gas bag into 24 layers with a thickness of 110 μm. The local emission coefficients are then derived by determining first the local emission of the most outer layer which is identical to the measured intensity at the edge of the gas-bag plasma. With this value the local emission of the next outer layer can be derived. This procedure is continued successively until the gas-bag center is reached.

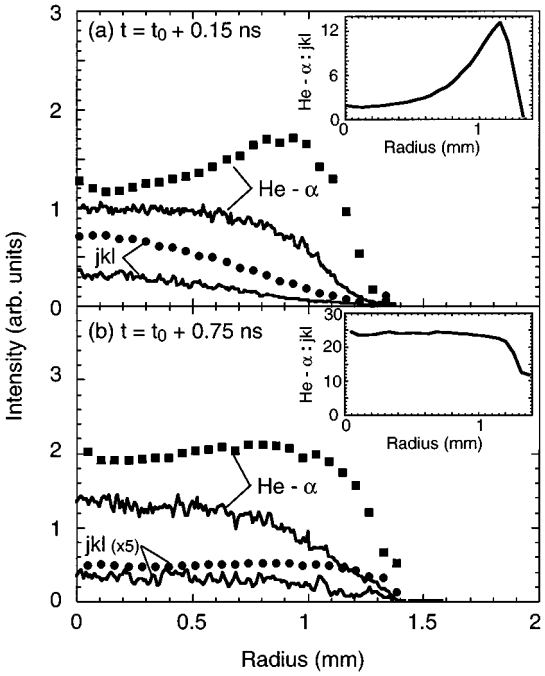

FIG. 7. Abel inversion for the He-α line and the j,k,l dielectronic satellites from a neopentane filled gas bag for $t=t_0+0.15$ ns (a) and $t=t_0+0.75$ ns (b). The lines (—) are the measured radial intensities. The dots are the local emission coefficients after Abel inversion (■: He-α; ●: j,k,l satellites). The insets show the electron temperature sensitive intensity ratio of the He-α transition to the j,k,l satellites. These type of measurements indicate a hot edge of the gas-bag plasma at early times and verify the good homogeneity of the gas-bag plasmas for $t>t_0+0.4$ ns and for radii $r<1$ mm.

Figure 7 shows examples of the measurements of the He-α and j,k,l dielectronic satellites as a function of the radius r of the gas bag at $t=t_0+0.15$ ns (a) and $t=t_0+0.75$ ns (b). The local emission coefficient at early times at $t=t_0+0.15$ ns shows a stronger He-α emission at the edge of the gas bag than in the center, while the j,k,l satellite emission shows the opposite behavior. The intensity ratio of the He-α line to the j,k,l satellites is plotted in the inset, and clearly reveals a cold core and a hot shell of the

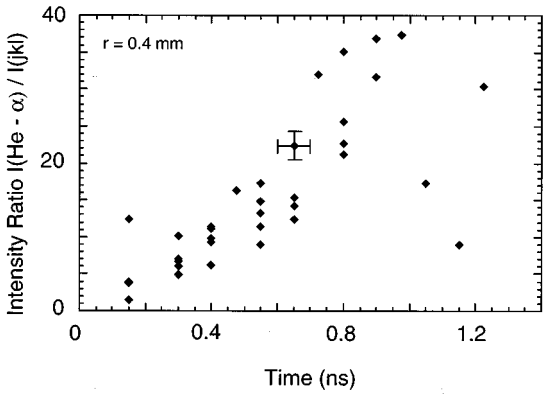

FIG. 8. Experimental ratios of the He-α line to the j,k,l dielectronic satellites of argon as a function of time at $r=0.4$ mm. The data are obtained from 15 shots with neopentane-filled gas bags.

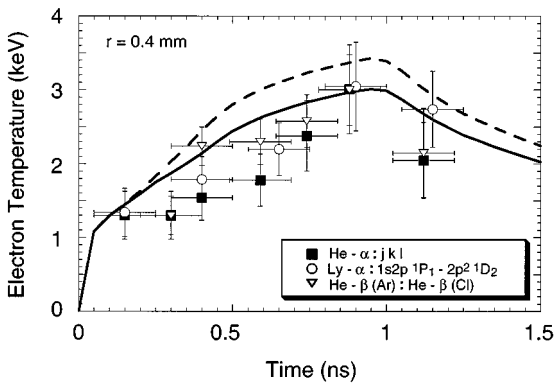

FIG. 9. Electron temperature as a function of time for neopentane-filled gas bags at $r=0.4$ mm. Experimental data of three line ratios are shown together with the results of hydrodynamic simulation. He-α to j,k,l satellites: ■; Ly-α to $1s2p\,^1P_1-2p^2\,^1D_2$ satellite: ○; He-β of Ar to the He-β of Cl: ∇. The uncertainties of the experimental data are about 20%. The horizontal error bar is 0.1 ns for all experimental data points. LASNEX simulations for 21-kJ heater beam energy: - - -; LASNEX simulations including the measured heater beam losses of 22% due to parametric instabilities (corresponding to 16.4-kJ effective heater beam energy): —.

gas-bag plasma. For $t=t_0+0.75$ ns the distribution of the local emission coefficients and the intensity ratio of the He-α line to the j,k,l satellites clearly show that the center of the plasma is homogeneous. When the plasma is homogeneous, i.e., for $t_0+0.40$ ns $<t<1.20$ ns, errors in the local line intensity ratios introduced by the Abel inversion are estimated to be about 5%.

Figure 8 shows the intensity ratio of the He-α line to the j,k,l satellites as a function of time at a radius of 0.4 mm after Abel inversion. Data from 15 shots with an incident laser energy of 21 ± 1 kJ are compiled in this plot. Typical errors for individual intensity ratios arising from the fitting procedure and the Abel inversion are about 15%, which is consistent with the reproducibility of the data. The large number of experimental data points allows us to deduce the electron temperature from the ratios shown in Fig. 8 independently of a simulated plasma evolution. This is achieved by iteratively determining the electron temperature history by time-dependent collisional-radiative modeling using FLY. The iteration is started with temperatures inferred from the experimental ratios by steady-state calculations. These starting values determine an electron temperature history of the plasma which is used in the first iteration of the time-dependent calculations. From the electron temperature history the temporal evolution of line intensity ratios is calculated and compared with the experimental ratios. After each iteration a new set of electron temperatures is used to derive new line intensity ratios. This procedure is repeated until no further changes of the electron temperatures are necessary to match the experimental line intensity ratios. For the line intensity ratios of the Ly-α line and respective dielectronic satellites as well as for the isoelectronic He-β lines of argon and chlorine, a difference of about 30% exists between steady-state and time-dependent calculations. For the He-α and j,k,l dielectronic satellites, the difference is only 4%, thus indicating the reliability of this ratio as a diagnostic of the electron temperature evolution of these plasmas.

For the calculations the electron density is chosen to be constant, i.e., $n_e=10^{21}$ cm^{-3} for neopentane-filled gas bags. This value is consistent with the intensity ratio of the intercombination line and the He-α line of argon (see Sec. III B) and with the measurement of the wavelength shift of stimulated Raman scattered laser light [1]. It is also consistent with the known fill density of the target. However, the exact value is not critical for the determination of the electron temperature. For example, steady-state collisional-radiative model calculations show that reducing the electron density by one order of magnitude affects the electron temperature determination by only about 5% (cf. Fig. 5).

The result of the iteration is plotted in Fig. 9 for a radius of $r=0.4$ mm together with calculated electron temperatures of the hydrodynamic code LASNEX [19]. Results of two simulations are shown. The dashed curve corresponds to a total delivered energy of 21 kJ in the heater beams. The full curve is the result of a simulation where heater beam losses are included. The sum of the losses by SBS and SRS sidescattering and backscattering were measured to be roughly constant for the duration of the heater beams, and account for 22% for a neopentane-filled gas bag. The inclusion of the heater beam losses in the simulations significantly improves the agreement between the experimental and calculated data. The simulated peak electron temperature of $k_BT_e=3$ keV is in excellent agreement with the experimental peak temperature of $k_BT_e=3.0\pm0.5$ keV. Deviations between the simulations and the experiment occur during the heating phase of the plasma. The simulations predict a faster heating of the gas bags than experimentally observed. The discrepancy might be due to uncertainties of the measured heater beam losses by SRS and SBS which have a reproducibility of about 30%. Further contributions to the lag may be due to the atomic cross sections and transition probabilities used in the time-dependent collisional-radiative modeling and due to the simplified heat transport model used in the LASNEX simulations.

In addition to the spectrum of the heliumlike resonance transition of argon, we also measured the electron temperature using the $1s2p\,^1P^\circ-2p^2\,^1D$ dielectronic satellite transition on the red wing of the Ly-α line of argon. Figure 10 shows an example of a high-resolution spectrum in the wavelength range 0.372 nm$<\lambda<$0.38 nm detected at $t=t_0+0.60$ ns. The two multiplet components of the Ly-α line at 0.3731

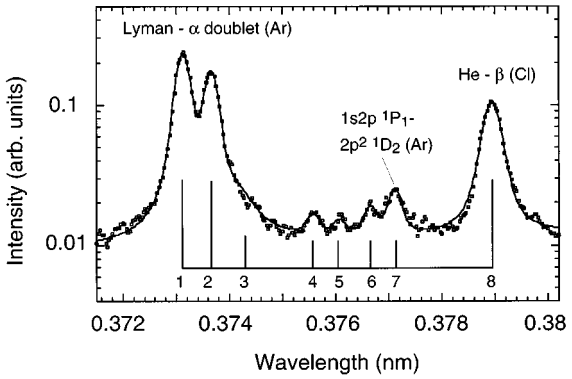

FIG. 10. High-resolution spectrum of the hydrogenlike resonance lines and dielectronic satellites of argon at $t=t_0+0.6$ ns. The spectrum represents emission averaged over 110 μm along the height of the gas-bag plasma (□). To determine the relative intensities of the spectral lines the spectrum was fit by eight lines (—). Transitions in argon: 1, Ly-α component or $1s\,^2S_{1/2}-2p\,^2P_{3/2}$; 2, Ly-$\alpha$ component or $1s\,^2S_{1/2}-2p\,^2P_{1/2}$; 3, $2s^2\,^1S_0-1s2p\,^1P_1$ and $n=3$ satellites; 4, $1s2s\,^1S_1-2s2p\,^1P_3$; 5, $1s2s\,^3S_1-2s2p\,^3P_2$; 6, $1s2p\,^3P_3-2p^2\,^3P_2$; 7, $1s2p\,^1P_1-2p^2\,^1D_2$. Transition in chlorine: 8, $1s^2\,^1S_0-1s3p\,^1P_1$.

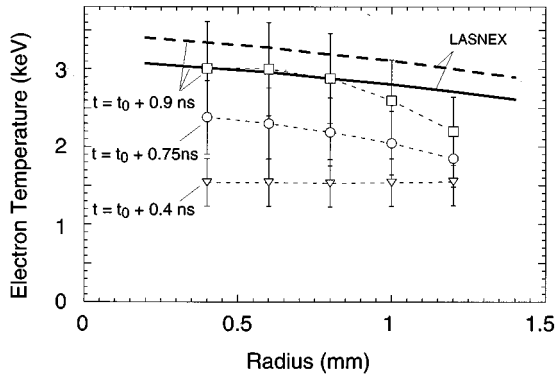

FIG. 11. Electron temperatures as a function of the radius of neopentane-filled gas bags after Abel inversion for $t=t_0+0.4$ ns, $t=t_0+0.75$ ns, and $t=t_0+0.9$ ns. The uncertainties of the experimental data are 20%. Also shown are LASNEX simulations at $t=t_0+0.9$ ns for 21-kJ heater beam energy (- - -) and for 16.4 kJ which corresponds to the measured effective heater beam energy (—).

and 0.3737 nm are clearly resolved. The intensity ratio of the components is density sensitive [56], and is consistent with 10^{21} cm^{-3}. On the spectrum of Fig. 10 several dielectronic satellite transitions can be seen, but only the $1s2p\,^1P°-2p^2\,^1D$ (0.3771 nm) satellite is measurable over a time interval that permits a temperature history to be extracted. The electron temperature from the relative intensity of this satellite to the Ly-α transition is also plotted in Fig. 9. We find good agreement between the electron temperatures inferred from the dielectronic satellite transitions of the He-α and Ly-α transition for the full time interval of Fig. 9. In particular, the peak temperatures agree within 5% demonstrating the mutual consistency of the temperature data.

Furthermore, the electron temperatures inferred from dielectronic satellite transitions are consistent with those using the isoelectronic line intensity ratio of the He-β lines, i.e., the $1s^2\,^1S_0-1s3p\,^1P°$ transitions in heliumlike ions, of argon and chlorine (see Fig. 4) which was first proposed for temperature measurements in Ref. [20]. The electron temperature evolution of the plasma obtained from this ratio is also plotted in Fig. 9. We find good agreement with the results of the other techniques. Within the uncertainties of about 20% the electron temperatures inferred from the various line ratios agree with each other. Small deviations occur at early times ($t_0+0.40$ ns$<t<t_0+0.60$ ns) between the dielectronic satellite technique and the isoelectronic technique. These deviations are probably due to the fact that in this time interval the He-β line is weak.

In Fig. 11 we show the electron temperatures as a function of the radius r of the plasma for $t=t_0+0.40$ ns, $t=t_0+0.75$ ns, and $t=t_0+0.90$ ns obtained from the He-α line and the j,k,l satellites. The center of gas bags with a diameter of 2 mm shows a homogeneous electron temperature distribution, for a time interval of $t_0+0.40$ ns $<t<t_0+1.10$ ns. For this time during the plasma evolution reliable experimental temperature data are obtained, with an error of about 20%. This estimate includes uncertainties in the determination of the line ratios after fitting the experimental spectra and performing the Abel inversion. The hot homogeneous center of the plasma shown in Fig. 11 is the region where all heater beams overlap and homogeneously heat the plasma. The electron temperature drops for radii larger than about $r=1$ mm. In this region the heater beams do not completely overlap, resulting in less energy absorption than in the central part of the plasma. Also shown in Fig. 11 are the results of LASNEX simulations for $t=t_0+0.90$ ns. In particular, the calculations which include heater beam energy losses compare well to the experimental data for $r<1$ mm. For larger radii the hydrodynamic simulations overestimate the electron temperature. This may be due to the two-dimensional approximation in the simulations which does not account for the lower effective heater beam intensities at the edge of the gas bags. For very early times $t<t_0+0.25$ ns hot regions at the edge of the plasma are found (cf. Fig. 7), and for times $t>t_0+1.10$ ns the intensities of some spectral lines become too low so that the results of the Abel inversion is affected by significant errors. Moreover, as seen in Fig. 8, the reproducibility of the experimental data is also reduced after 1.10 ns. For these reasons we do not give temperature data for $t<t_0+0.25$ ns and $t>t_0+1.10$ ns.

Peak electron temperatures for various gas fills are summarized in Fig. 12. Besides C_5H_{12}, data are shown from C_3H_8, CO_2, and CF_4, and a mixture of the latter two gases. These gases were used in Ref. [11] to vary electron and ion Landau damping of the plasmas. For the time-dependent collisional-radiative modeling we used electron densities calculated from the number of electrons in the bag. To rule out uncertainties we monitored the gas pressure of each target with a pressure transducer just prior to the laser shot. Again the calculated density is consistent with density sensitive line ratios as well as with spectra from stimulated Raman scattering, and is not critical for the determination of the electron temperature. The temperature evolution and the peak values are similar to those of neopentane-filled gas bags. The peak temperatures are reached later in time by about 0.20 ns. The temperature gradually increases with higher densities of the target. In Fig. 12 we plot the peak temperatures versus the ratio of the electron to the critical density of a 351.1-nm laser beam. The observed temperature scaling is consistent with

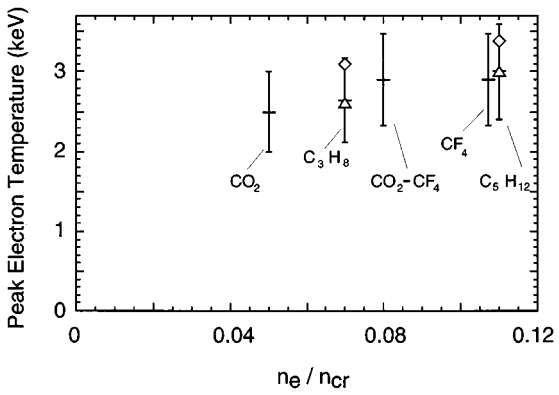

FIG. 12. Peak electron temperatures of gas bags filled with various gases as a function of electron density, experimental data: +. Also shown are results of LASNEX simulations for propane and neopentane calculated for a heater beam energy of 21 kJ: ◇; and for a reduced heater beam energy of 16.4 kJ for neopentane and 14.5 kJ for propane to account for heater beam losses by parametric instabilities: △. The uncertainties of the experimental data are 20%. The calculational results which account for heater beam energy losses agree well with the experiments.

our understanding of inverse bremsstrahlung absorption. For example, detailed LASNEX simulations for propane with 21-kJ heater beam energy result in a 10% lower peak temperature than for neopentane. Including the measured heater beam losses of 31% for propane and 22% for neopentane gives a 13% lower peak temperature for propane filled gas bags than for neopentane, which is in excellent agreement with the experiment.

B. Electron density

In this section we investigate the consistency of the line intensity ratio of the intercombination line ($1s^2\,{}^1S$–$1s2p\,{}^3P°$) to the resonance transition (He-α) of heliumlike argon with the electron densitites we expect from the fill densities of the gas bags. This ratio is density sensitive, and also shows some dependence on the electron temperature. This is demonstrated in Fig. 13 where the results of steady-state collisional-radiative model calculations are shown. The line ratio is sensitive to electron density variations because the radiative decay rate of the triplet level is much smaller than that of the singlet level. With increasing electron densities the electron collisional depopulation rate of the triplet level assumes the same order as its radiative decay rate. Hence the relative upper state population and relative intensity of the intercombination line decreases compared to the resonance line which upper level is predominantly depopulated by radiative decay.

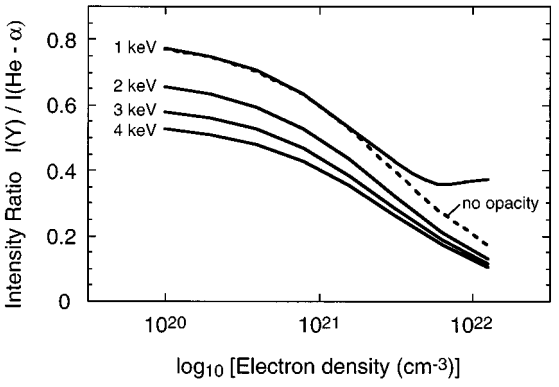

FIG. 13. Steady-state collisional-radiative model calculations for the line intensity ratio of the $1s^2\,{}^1S$–$1s2p\,{}^3P°$ intercombination (or Y) line to the He-α transition of argon as a function of the electron density for $T_e=1$ keV, $T_e=2$ keV, $T_e=3$ keV, and $T_e=4$ keV [42]. While for $T_e=1$ keV the ratio is affected by self-absorption effects, there are no effects for larger temperatures.

From two-dimensional x-ray images of gas bags we find that for $t<t_0+1.50$ ns no significant rarefaction or deviations of the plasma from a spherical symmetry occur (cf. Fig. 2). For that reason it was assumed that the electron density of the plasma is simply given by the number of electrons of the gas filling and its pressure giving, e.g., $n_e=10^{21}$ cm^{-3} for neopentane. However, deviations from a homogeneous electron density distribution of the plasma are expected to occur in the shock front which is launched by the explosion of the membrane (cf. Fig. 3). Our measurements and calculations indicate that the perturbations due to the shock are significantly reduced for the 0.22-μm-thick membranes employed here. In the present study a density peak of $n_e=2\times10^{21}$ cm^{-3} in a 100-μm-thick shell moving approximately with the sound speed towards gasbag center is predicted by LASNEX simulations.

Figure 14 shows the experimental intensity ratio of the intercombination to the resonance transition averaged over five measurements for three radii, $r=0.4$, 0.8, and 1.2 mm. For $r=0.4$ mm no deviations of the electron density from $n_e=10^{21}$ cm^{-3} are expected, because the shock does not reach this radius in the time interval shown in Fig. 14. For this reason we compare the measured line intensity ratios with calculated ratios employing the experimental electron temperature history obtained in Sec. III A, and assume that a constant electron density of $n_e=10^{21}$ cm^{-3} is produced within about 0.20 ns. We find quite good agreement between the calculated and the experimental ratios [Fig. 14(a)]. For $t<0.25$ ns the experimental and calculated ratios assume a value of about 0.7, which gradually reduces to 0.3 for 0.25 ns $<t<1.20$ ns.

In addition, for a radius of $r=0.8$ mm the calculations are in fair agreement with the experiment. In this case, our LASNEX simulations show that the shock front with a density of $n_e=2\times10^{21}$ cm^{-3} arrives at $t\approx t_0+0.80$ ns. The ratio is calculated assuming that a density of $n_e=10^{21}$ cm^{-3} is produced within $t=t_0+0.20$ ns, and perturbed at $t=t_0+0.80$ ns for a duration of 0.15 ns. For that reason the calculated ratio shows a kink at $t\approx t_0+0.80$ ns, giving a minimum ratio of 0.2. Since the width of the shock is only about 100 μm, the present spectroscopic measurements and the Abel inversion technique is not sufficiently sensitive to resolve this perturbation. However, the calculations are within the uncertainties of the experimental data [Fig. 14(b)].

For a radius of $r=1.2$ mm, where the laser beams heat the plasma first, the experimental intensity ratios differ from the data obtained further inside of the gas bag. A constant intensity ratio occurs of about 0.3 for 0.20 ns $<t<1.20$ ns. A comparison with time-dependent collisional-radiative modeling is performed assuming that within $t<t_0+0.30$ ns a density of $n_e=2\times10^{21}$ cm^{-3} is produced, decreasing within

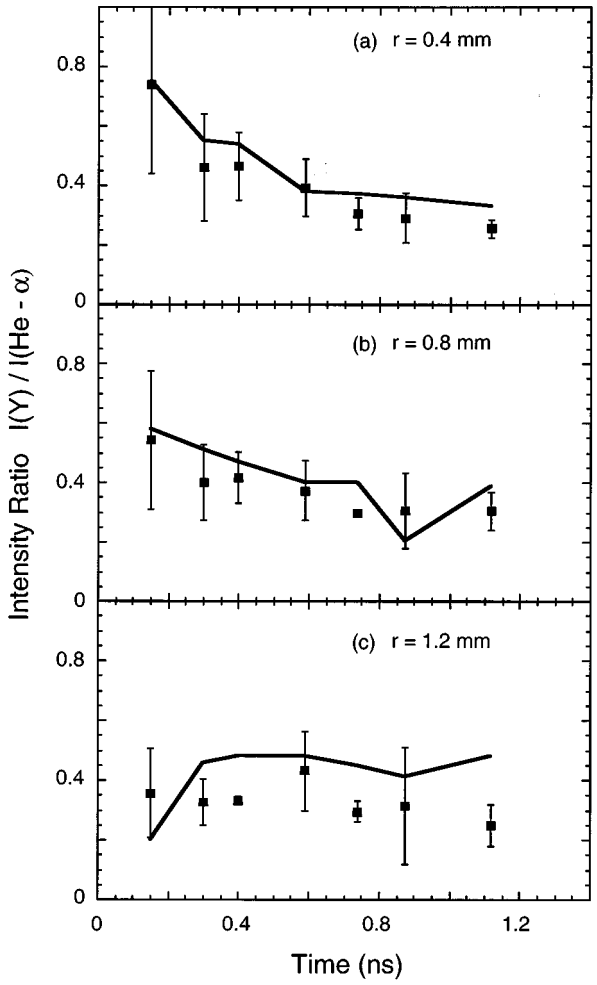

FIG. 14. Electron density sensitive line ratio Y ($1s^2\,{}^1S-1s2p\,{}^3P°$)/He-α ($1s^2\,{}^1S-1s2p\,{}^1P°$) of argon (■) as a function of time for three positions in a $C_5\,H_{12}$ filled gas bag: $r=0.4$ mm (a), $r=0.8$ mm (b), and $r=1.2$ mm (c). The horizontal error bar is 0.1 ns for all experimental data points. The experimental ratios are compared with calculations (—) for a density of $n_e=10^{21}$ cm^{-3} and a perturbation of about 0.1-ns duration included in (b) and (c) due to the shock. For a radius of $r=0.4$ mm (a) a shock perturbation occurs at $t>1.4$ ns, and is therefore neglected. At $t\approx0.8$ ns the shock reached the radius of $r=0.8$ mm, causing a sharp decrease of the calculated ratio. At a radius of $r=1.2$ mm (c) the shock causes a significantly smaller ratio at $t\approx0.2$ ns as compared to (a) and (b).

0.10 ns to $n_e=10^{21}$ cm^{-3}, and remains constant for $t>t_0+0.40$ ns. Included in the calculations is the fact that the electron temperature history differs from those further inside of the gas bag; in particular, the peak temperature is only 2.2 keV (cf. Fig. 11). We find reasonable agreement between the experimental and calculated ratios.

Although reasonable agreement is obtained for all radii within the experimental errors, the calculations are consistently slightly greater than the experimental mean values. These small deviations may be due to suprathermal electrons which influence the electron collisional excitation and reduce the population density of the $1s2p\,{}^3P°$ triplet level. These suprathermal electrons reduce the intensity of the intercombination line and therefore lead to a smaller intensity ratio. Although, this effect is not included in our collisional-radiative modeling, calculations for the line intensity ratio of the intercombination to the resonance line of argon have been performed in Ref. [27]. For the present densities, these calculations indicate that the intensity ratio is reduced by hot electron excitation of the intercombination line by about 10–20 %. Taking this correction into account improves the agreement between the experimental and calculated ratios.

IV. CONCLUSIONS

We applied accurate spectroscopic techniques to benchmark hydrodynamic simulations of inertial confinement fusion plasmas. Our temporally and spatially resolved spectroscopic electron temperature and density measurements of neopentane-filled gas bags show a peak temperature of $k_BT_e=3$ keV, and densities of $n_e=10^{21}$ cm^{-3}. Further gas fills have been investigated, and slightly lower temperatures are observed for lower gas densities. These findings are in agreement with two-dimensional hydrodynamic simulations using LASNEX. In particular, we take into account heater beam energy losses by SBS and SRS sidescattering and backscattering which results in calculated peak temperatures that are within 3% of those measured in the experiment, demonstrating our ability to simulate high-temperature large scale-length laser-produced plasmas. Furthermore, the experimentally observed homogeneous plasma center is in agreement with the simulations. However, discrepancies are observed when comparing the measured temporal evolution of the temperature of the plasma with the details of the simulations. The experimental results show that the plasma heats more slowly than calculated. This observation might be related to uncertainties in the measurement of the heater beam energy losses, to uncertainties in the time-dependent collisional-radiative modeling or to the simplified heat transport model used in the LASNEX simulations.

ACKNOWLEDGMENTS

We would like to thank the Nova crew for their efforts, and B. Boggs, R. Costa, and D. Gemmel for their technical support. Many helpful discussions with R. W. Lee are gratefully acknowledged. This work was performed under the auspices of the U.S. Department of Energy by the Lawrence Livermore National Laboratory under Contract No. W-7405-ENG-48.

[1] B. J. MacGowan, B. B. Afeyan, C. A. Back, R. L. Berger, G. Bonnaud, M. Casanova, B. I. Cohen, D. E. Desenne, D. F. Dubois, A. G. Dulieu, K. G. Estabrook, J. C. Fernandez, S. H. Glenzer, D. E. Hinkel, D. H. Kalantar, R. L. Kauffman, R. K. Kirkwood, W. L. Kruer, A. B. Langdon, B. F. Lasinski, D. S. Montgomery, J. D. Moody, D. H. Munro, L. V. Powers, H. A. Rose, C. Rousseaux, R. E. Turner, B. H. Wilde, S. C. Wilks, and E. A. Williams, Phys. Plasmas **3**, 2029 (1996).

[2] L. V. Powers, R. E. Turner, R. L. Kauffman, R. L. Berger, P. A. Amendt, C. A. Back, T. P. Bernat, S. N. Dixit, D. I. Eimerl,

J. A. Harte, M. A. Henesian, D. H. Kalantar, B. F. Lasinski, B. J. MacGowan, D. S. Montgomery, D. H. Munro, D. M. Pennington, T. D. Shepard, G. F. Stone, L. J. Suter, and E. Williams, Phys. Rev. Lett. **74**, 2957 (1995); L. V. Powers, R. L. Berger, R. L. Kauffman, B. J. MacGowan, P. A. Amendt, C. A. Back, T. P. Bernat, S. N. Dixit, D. I. Eimerl, K. G. Estabrook, J. A. Harte, D. H. Kalantar, D. E. Klem, B. F. Lasinski, D. S. Montgomery, J. D. Moody, D. H. Munro, T. D. Shepard, L. J. Suter, R. E. Turner, and E. Williams, Phys. Plasmas **2**, 2473 (1995).

[3] W. L. Kruer, *The Physics of Laser Plasma Interactions* (Addison-Wesley, New York, 1988).

[4] H. A. Baldis, E. M. Campbell, and W. L. Kruer, in *Physics of Laser Plasma*, Vol. 3, edited by A. Rubenchik and S. Witkowski (North-Holland, Amsterdam, 1991), pp. 361–434.

[5] J. Lindl, Phys. Plasmas **2**, 3933 (1995).

[6] S. W. Haan, S. M. Pollaine, J. D. Lindl, L. J. Suter, R. L. Berger, L. V. Powers, W. E. Alley, P. A. Amendt, J. A. Futterman, W. K. Levedahl, M. D. Rosen, D. P. Rowley, R. A. Sacks, A. I. Shestakov, G. L. Strobel, M. Tabak, S. V. Weber, G. Zimmerman, W. J. Krauser, D. C. Wilson, S. V. Coggeshall, D. B. Harris, N. M. Hoffman, and B. H. Wilde, Phys. Plasmas **2**, 2480 (1995).

[7] R. L. Kauffman, in *Physics of Laser Plasma*, Vol. 3, edited by A. Rubenchik and S. Witkowski (North-Holland, Amsterdam, 1991), pp. 111–162; V. A. Boiko, A. V. Vinogradov, S. A. Pikuz, I. Yu. Skobelev, and A. Ya. Faenov, Itogi Nauki Tekh. Ser. Radiotekh. **27**, 10 (1980) [J. Sov. Laser Res. **6**, 85 (1985)]; C. De Michelis and M. Mattioli, Nucl. Fusion **21**, 677 (1981).

[8] C. A. Back *et al.* (unpublished).

[9] C. J. Keane, B. A. Hammel, A. L. Osterheld, and D. R. Kania, Phys. Rev. Lett. **72**, 3029 (1994).

[10] J. D. Moody, B. J. MacGowan, R. K. Kirkwood, and D. S. Montgomery, Rev. Sci. Instrum. (to be published).

[11] D. S. Montgomery, B. B. Afeyan, B. J. MacGowan, C. A. Back, S. H. Glenzer, R. K. Kirkwood, J. D. Moody, G. F. Stone, R. L. Berger, K. G. Estabrook, W. L. Kruer, B. F. Lasinski, D. H. Munro, E. A. Williams, D. Desenne, and C. Rousseaux (unpublished).

[12] R. K. Kirkwood, B. B. Afeyan, W. L. Kruer, B. J. MacGowan, J. D. Moody, D. S. Montgomery, D. M. Pennington, T. L. Weiland, and S. C. Wilks, Phys. Rev. Lett. **76**, 2065 (1996).

[13] D. H. Kalantar, B. J. MacGowan, T. P. Bernat, D. E. Klem, W. W. Hsing, and B. Failor, Rev. Sci. Instrum. **66**, 782 (1995); D. H. Kalantar, D. E. Klem, B. J. MacGowan, J. D. Moody, D. S. Montgomery, D. H. Munro, T. D. Shepard, G. F. Stone, B. J. Failor, W. W. Hsing, Phys. Plasmas **2**, 3161 (1995).

[14] C. A. Back, R. L. Berger, K. Estabrook, B. H. Failor, W. W. Hsing, E. J. Hsieh, R. Hockaday, D. H. Kalantar, R. L. Kauffman, C. J. Keane, D. E. Klem, B. J. MacGowan, D. S. Montgomery, J. D. Moody, L. V. Powers, T. D. Shepard, G. F. Stone, L. J. Suter, and R. E. Turner, J. Quantum Spectrosc. Radiat. Transfer **54**, 27 (1995).

[15] B. H. Failor, W. W. Hsing, R. G. Hockaday, T. D. Shepard, D. E. Klem, D. H. Kalantar, and B. J. MacGowan, Rev. Sci. Instrum. **66**, 767 (1995).

[16] T. Shepard, C. A. Back, D. H. Kalantar, R. L. Kauffman, C. J. Keane, D. E. Klem, B. F. Lasinski, B. J. MacGowan, L. V. Powers, L. J. Suter, R. E. Turner, B. H. Failor, and W. W. Hsing, Rev. Sci. Instrum. **66**, 749 (1995); Phys. Rev. E **53**, 5291 (1996).

[17] A. H. Gabriel, Mon. Not. R. Astron. Soc. **160**, 99 (1972).

[18] U. I. Safronova, M. S. Safronova, and R. Bruch, J. Phys. B **28**, 2803 (1995).

[19] G. B. Zimmerman and W. L. Kruer, Comments Plasma Phys. Controlled Fusion **2**, 85 (1975).

[20] R. S. Majoribanks, M. C. Richardson, P. A. Jaanimagi, and R. Epstein, Phys. Rev. A **46**, 1747 (1992); R. S. Majoribanks, F. Budnik, G. Kulcsár, and L. Zhao, Rev. Sci. Instrum. **66**, 683 (1995).

[21] C. A. Back, D. H. Kalanter, R. L. Kauffman, R. W. Lee, B. J. MacGowan, D. S. Montgomery, L. V. Powers, T. D. Shepard, G. F. Stone, and L. J. Suter, Phys. Rev. Lett. (to be published); C. A. Back, S. H. Glenzer, R. W. Lee, B. J. MacGowan, J. C. Moreno, J. K. Nash, L. V. Powers, and T. D. Shepard in *Atomic Processes in Plasmas*, edited by A. Osterheld and W. Goldstein, AIP Conf. Proc. No. 381 (AIP, New York, 1996), pp. 123–130.

[22] H.-J. Kunze, A. H. Gabriel, and H. R. Griem, Phys. Fluids **11**, 662 (1968).

[23] V. A. Boiko, S. A. Pikuz, and A. Ya. Faenov, J. Phys. B **12**, 1889 (1979).

[24] E. V. Aglitskii, V. A. Boiko, A. V. Vinogradov, and E. A. Yukov, Kvant. Elektron. (Moscow) **1**, 579 (1974) [Sov. J. Quantum Electron. **4**, 322 (1974)].

[25] K. N. Koshelev, Yu. V. Sidelnikov, G. Decker, V. Kies, M. Malzig, P. Rowekamp, F. Rosmej, A. Schulz, and H.-J. Kunze, Opt. Spectrosc. **76**, 198 (1994).

[26] A. Schulz and K. N. Koshelev, J. Quantum Spectrosc. Radiat. Transfer **54**, 361 (1995).

[27] F. B. Rosmej, O. N. Rosmej, S. A. Komarov, V. O. Mishensky, and J. G. Utjugov, in *Dense Z-Pinches*, edited by M. Haines and A. Knight, AIP Conf. Proc. No. 299 (AIP, New York, 1993), pp. 552–559.

[28] G. Charatis, D. C. Slater, F. J. Mayer, J. A. Tarvin, G. E. Busch, D. Sullivan, D. Musinski, D. L. Matthews, and L. Koppel, in *Low Energy X-ray Diagnostics*, edited by D. T. Attwood and B. L. Henke, AIP Conf. Proc. No. 75 (AIP, New York, 1981), pp. 270–274.

[29] E. M. Campbell, J. T. Hunt, E. S. Bliss, D. R. Speck, and R. P. Drake, Rev. Sci. Instrum. **57**, 2101 (1986).

[30] M. D. Rosen and J. H. Nuckolls, Phys. Fluids **22**, 1393 (1979); R. A. London and M. D. Rosen, *ibid.* **29**, 3813 (1986).

[31] J. Denavit and D. W. Phillion, Phys. Plasmas **1**, 1971 (1994).

[32] A. B. Langdon, Phys. Rev. Lett. **44**, 575 (1980).

[33] C. A. Back, R. L. Kauffman, P. M. Bell, and J. D. Kilkenny, Rev. Sci. Instrum. **66**, 764 (1995).

[34] J. D. Kilkenny, Laser Part. Beams **9**, 49 (1991).

[35] F. Ze, R. L. Kauffman, J. D. Kilkenny, J. Weidwald, P. M. Bell, R. Hanks, J. Steward, D. Dean, J. Bauer, and R. Wallace, Rev. Sci. Instrum. **63**, 5124 (1992).

[36] P. M. Bell, J. D. Kilkenny, G. Power, R. Bonner, and K. Bradley, Proc. SPIE **1155**, 430 (1989).

[37] B. D. Fried, R. B. White, T. K. Samec, Phys. Fluids **14**, 2388 (1971); R. J. Huck and E. A. Johnson, Phys. Rev. Lett. **44**, 142 (1980); E. A. Williams, R. L. Berger, R. P. Drake, A. M. Rubenchik, B. S. Bauer, D. D. Meyerhofer, A. C. Gaeris, and T. W. Johnston, Phys. Plasmas **2**, 129 (1995).

[38] O. L. Landen, P. M. Bell, J. A. Ortel, J. J. Satariano, and D. K. Bradley, in *Ultrahigh- and High-Speed Photography, Video-*

graphy, and Photonics (SPIE, Bellingham, WA, 1993), Vol. 2002, p. 2.
[39] B. L. Henke, E. M. Gullikson, and J. C. Davis, At. Data Nucl. Data Tables **54**, 331 (1993).
[40] R. L. Kelly, J. Phys. Chem. Ref. Data **16**, Suppl. 1 (1987).
[41] V. A. Boiko, A. Ya. Faenov, and S. A. Pikuz, J. Quantum Spectrosc. Radiat. Transfer **19**, 11 (1978).
[42] R. W. Lee, B. L. Whitten, R. E. Strout II, J. Quantum Spectrosc. Radiat. Transfer **32**, 91 (1984); R. W. Lee (private communication).
[43] U. Feldman, G. A. Doschek, D. J. Nagel, R. D. Cowan, and R. R. Whitlock, Astrophys. J. **192**, 213 (1974).
[44] E. A. Kononov, K. N. Koshelev, and Yu. V. Sidelnikov, Fiz. Plazmy **11**, 927 (1985) [Sov. J. Plasma Phys. **11**, 538 (1985)]; K. N. Koshelev and N. R. Pereira, J. Appl. Phys. **69**, R21 (1991).
[45] J. F. Seely and T. N. Lee, Phys. Rev. A **29**, 411 (1984).
[46] C. P. Bhalla, A. H. Gabriel, and L. P. Presnyakov, Mon. Not. R. Astron. Soc. **172**, 359 (1975).
[47] L. A. Vainshtein and U. I. Safronova, At. Data Nucl. Data Tables **21**, 49 (1978).
[48] D. H. Sampson, S. J. Goett, and R. E. H. Clark, At. Data Nucl. Data Tables **28**, 299 (1983); H. Zhang, D. H. Sampson, and R. E. H. Clark, *ibid.* **35**, 267 (1986).
[49] A. H. Gabriel and T. M. Paget, J. Phys. B **5**, 673 (1972).
[50] P. Beiersdorfer, A. L. Osterheld, T. W. Phillips, M. Bitter, K. W. Hill, and S. von Goeler, Phys. Rev. E **52**, 1980 (1995).
[51] F. B. Rosmej, J. Phys. B **28**, L747 (1995); J. Quantum Spectrosc. Radiat. Transfer **51**, 319 (1994).
[52] E. Träbert and F. C. Fawcett, J. Phys. B **12** L441 (1979); I. A. Armour, F. C. Fawcett, J. D. Silver, and E. Träbert, Phys. Rev. B **13**, 2701 (1980); E. Träbert, F. C. Fawcett, and J. D. Silver, J. Phys. B **15**, 3587 (1982).
[53] F. B. Rosmej, B. A. Bryunetkin, A. Ya. Faenov, I. Yu. Skobelev, M. P. Kalashnikov, P. V. Nickles, and M. Schnürer, J. Phys. B **29**, L299 (1996).
[54] F. Walden and H.-J. Kunze (private communication).
[55] N. J. Peacock, M. G. Hobby, and M. Galanti, J. Phys. B **6**, L298 (1974).
[56] J. P. Apruzese, J. Davis, D. Duston, and R. W. Clark, Phys. Rev. A **29**, 246 (1984); N. N. Ljepojevic, R. W. P. McWhirter, and S. Volonté, J. Phys. B **15**, 3285 (1985); T. Nash, C. Deeney, M. Krishnan, R. R. Prasad, P. D. Lepell, and L. Warren, J. Quantum Spectrosc. Radiat. Transfer **44**, 485 (1990).